# Aromatic ring dynamics, thermal activation and transient conformations of a 468 kDa enzyme by specific $^{1}H$-$^{13}C$ labeling and fast-MAS NMR

Diego F. Gauto,[1] Pavel Macek,[1] Alessandro Barducci,[2,*] Hugo Fraga,[1,3] Audrey Hessel,[1] Tsutomu Terauchi,[4,5] David Gajan,[6] Yohei Miyanoiri,[7,8] Jerome Boisbouvier,[1] Roman Lichtenecker,[9] Masatsune Kainosho[4,8,*] and Paul Schanda[1,*]

[1] Univ. Grenoble Alpes, CEA, CNRS, Institut de Biologie Structurale (IBS), 71, avenue des martyrs, F-38044 Grenoble, France.
[2] Centre de Biochimie Structurale (CBS), INSERM, CNRS, Université de Montpellier, Montpellier, France
[3] Departamento de Biomedicina, Faculdade de Medicina da Universidade do Porto, Porto, Portugal; i3S, Instituto de Investigação e Inovação em Saúde, Universidade do Porto, Portugal.
[4] Graduate School of Science, Tokyo Metropolitan University, 1-1 Minami-ohsawa, Hachioji, Tokyo 192-0397, Japan.
[5] SI Innovation Center, Taiyo Nippon Sanso Corp., 2008-2 Wada, Tama-city, Tokyo 206-0001, Japan.
[6] Université de Lyon, Centre de RMN à Hauts Champs de Lyon CRMN, FRE 2034, Université de Lyon, CNRS, ENS Lyon, UCB Lyon 1, 69100 Villeurbanne, France.
[7] Institute of Protein Research, Osaka University, 3-2 Yamadaoka, Suita, Osaka 565-0871, Japan.
[8] Structural Biology Research Center, Graduate School of Sciences, Nagoya University, Furo-cho, Chikusa-ku, Nagoya 464-8602, Japan.
[9] Institute of Organic Chemistry, University of Vienna, Währinger Str. 38, 1090 Vienna, Austria.

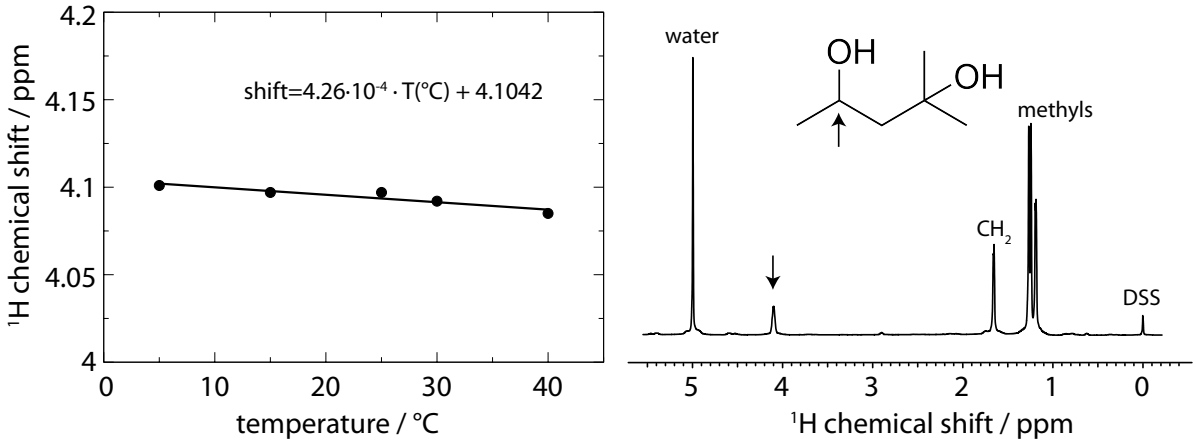


Figure S1. The use of 2-methyl-2,4-pentanediol (MPD) as a temperature sensor in NMR. Shown is the chemical shift of the CH signal at ca. 4.1 ppm as a function of temperature. The panel on the right shows the annotated spectrum at 5°C. The position of the peak highlighted with an arrow is plotted on the left and has been used to measure the temperature in our MAS NMR rotors.
The data were obtained from solution-NMR measurements using a 600 MHz Agilent VNMRS spectrometer with a room-temperature protein on a sample containing MPD and 4,4-dimethyl-4-silapentane-1-sulfonic acid (DSS) in $D_2O$ (with traces of $H_2O$).

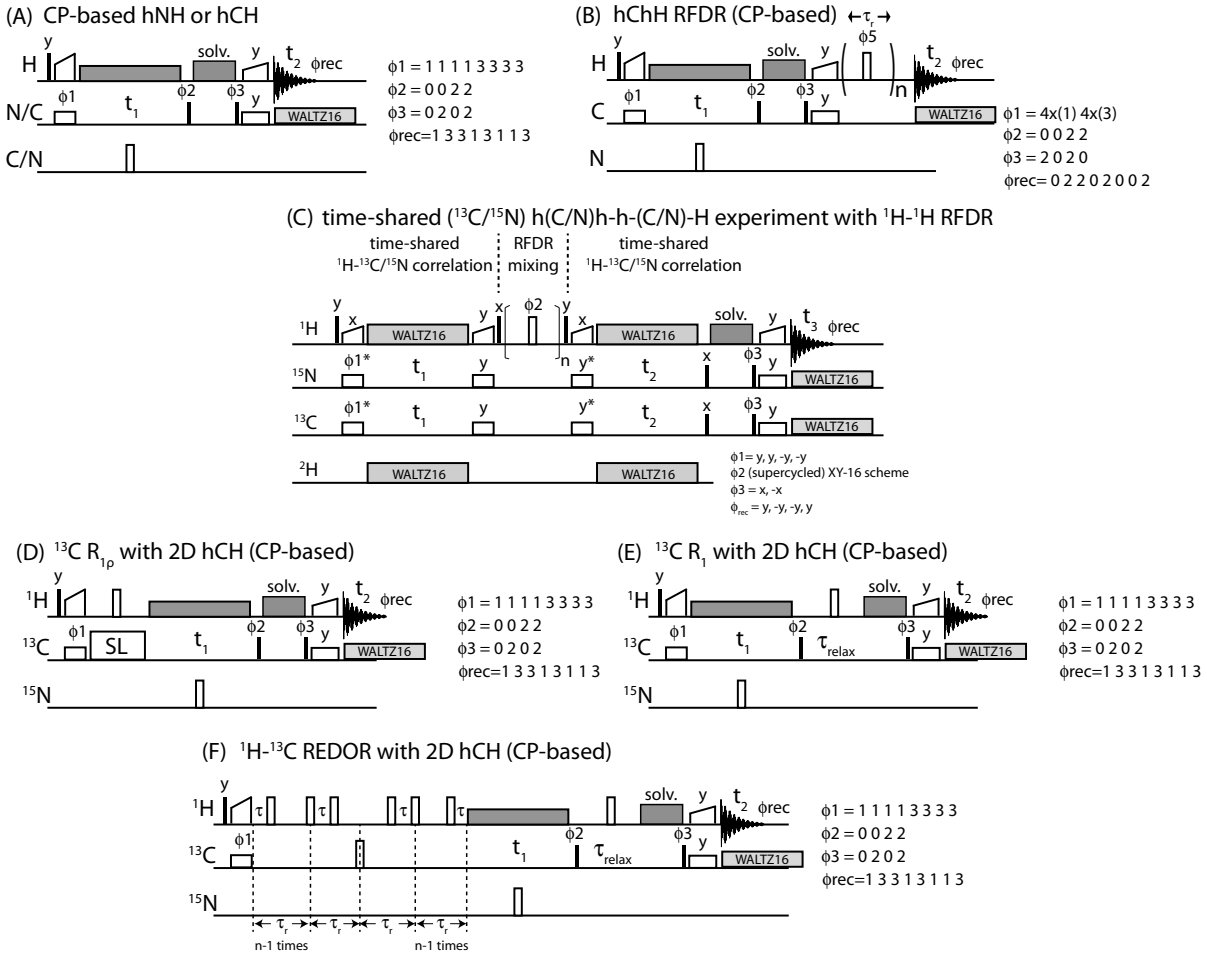


Figure S2. Pulse sequences employed in this study, akin to previously proposed ones (*1–4*). Narrow filled and open rectangles denote 90° and 180° pulses, respectively. Phases of pulses are x unless indicated otherwise (on the right of each sequence, where 0=x,1=y,2=-x,3=-y). In the REDOR experiment in panel (F) the REDOR pulses are cycled according to XY8 in a mirror-symmetric manner (before/after the central $\pi$ pulse, as detailed in reference (*3*).

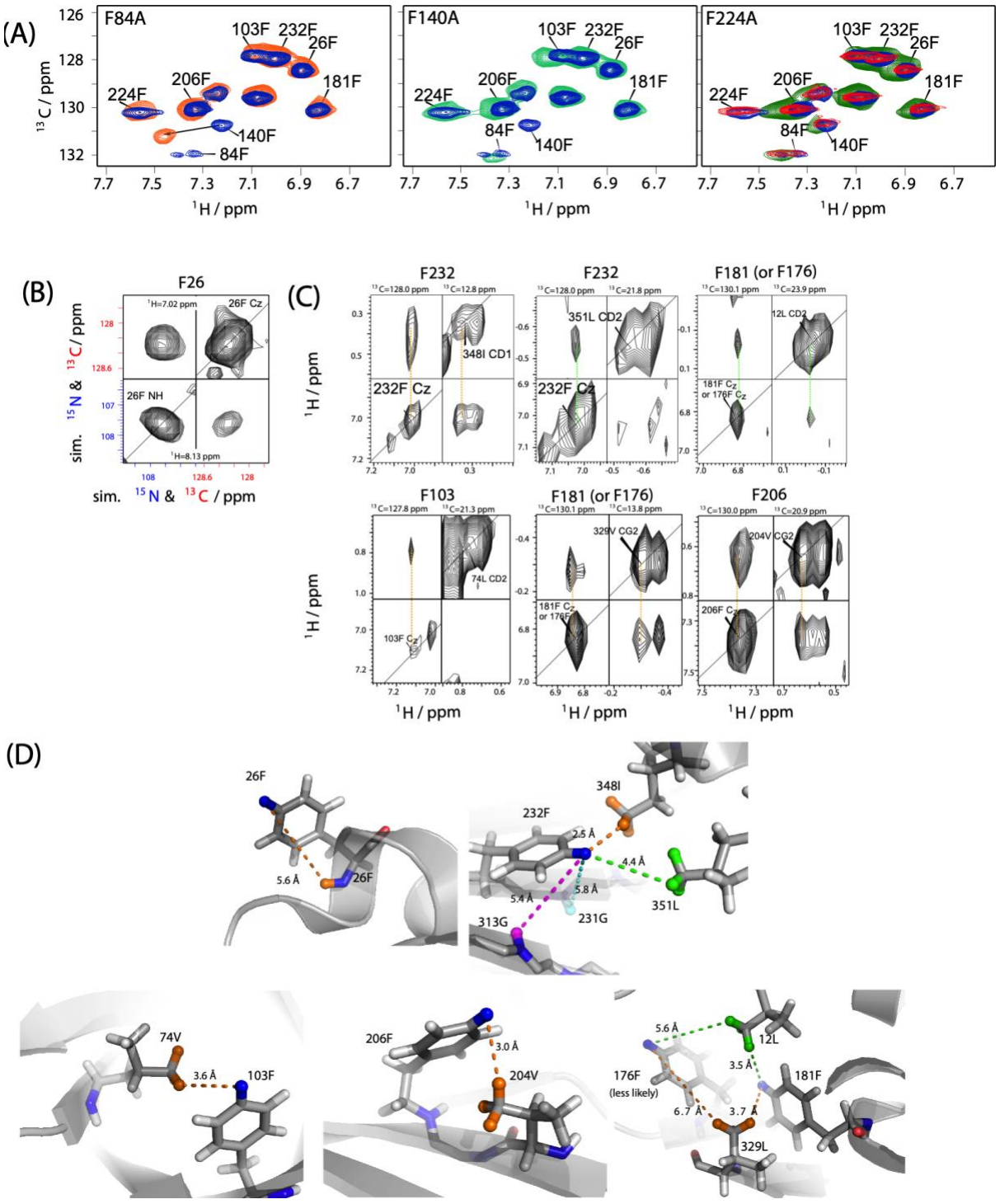


Figure S3. Assignment of *para*-CH sites in TET2 from mutagenesis and through-space dipolar transfer. (A) Cross-polarization-based HC correlation spectra of three single-point mutants of TET2 (F84A, F140A and F224A) overlaid with the wild-type spectrum (blue). Note that F84 and F140 are in close contact, such that mutation also leads to detectable chemical-shift change, as indicated in the left spectrum with an arrow. In the right panel, two different spectra of wild-type protein are shown in blue and red, respectively. The aim of this display is particularly to highlight that the apparent doubling of the peak of F84 (see also Figure 1 of the main text) is not always reproducible; however, its weak intensity is reproducible, likely related to conformational exchange, as detected by relaxation dispersion experiments (Figure4).
(B) and (C) show diagonal and cross-peaks between *para*-CH sites and backbone amide and methyl sites. Panel (B) shows data from a three-dimensional experiment with two time-shared $^{13}$C/$^{15}$N

heteronuclear dimensions (Figure S2C), akin to a sequence reported elsewhere (*1*); the experimental data in (C) employed only one heteronuclear dimension and two $^{1}$H dimensions, also as reported in reference (*1*), and Figure S2B. All detected distance restraints involving para-CH sites are displayed in panel (D).

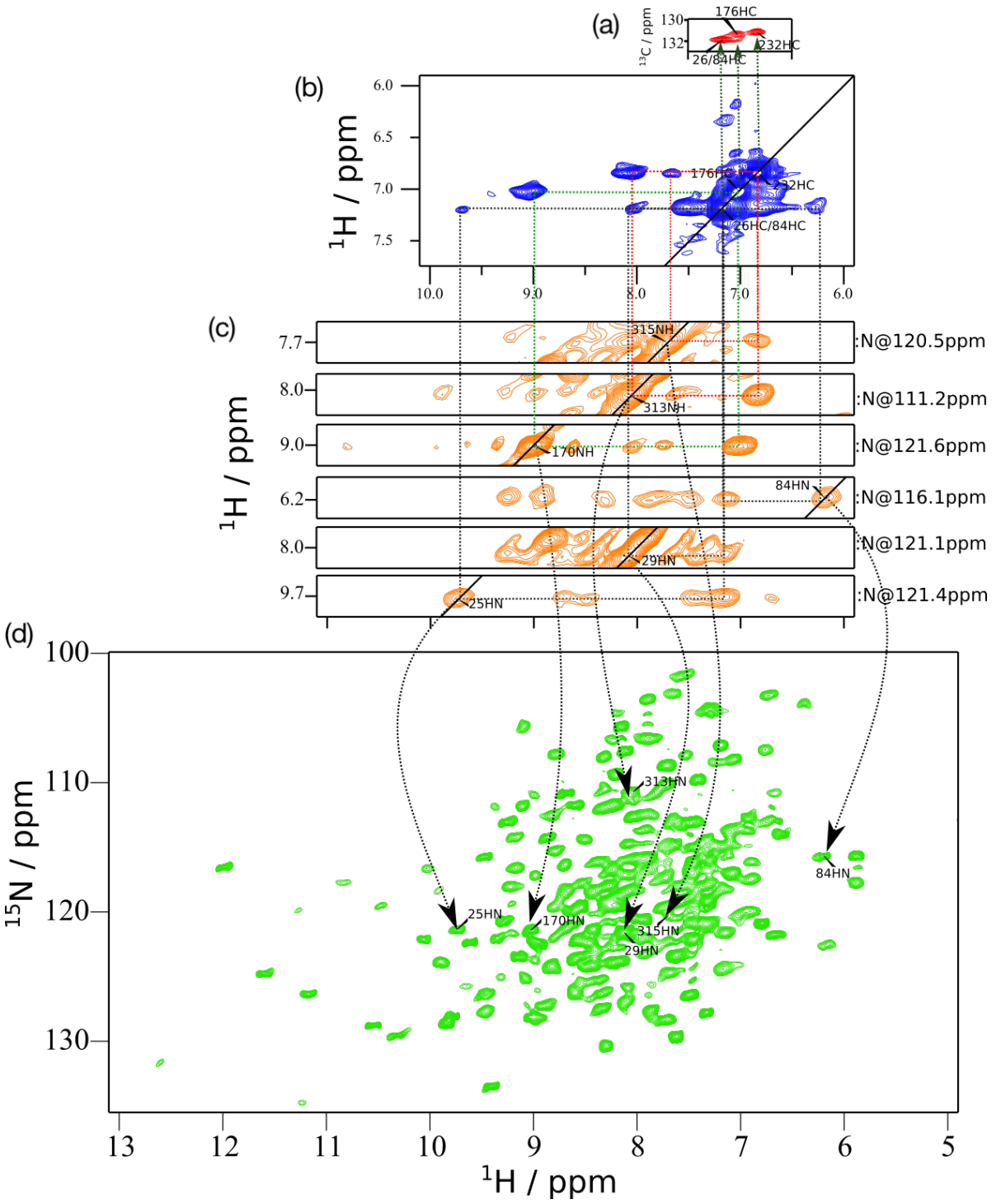


Figure S4. Assignment of Phe *ortho*-CH sites in TET2 *via* through-space contacts. (a) $^{1}$H-$^{13}$C correlation spectrum of *ortho*-CH labelled TET2. (b) Two-dimensional $^{1}$H-$^{1}$H RFDR correlation experiment, performed with the $^{13}$C-filtered pulse sequence shown in Figure S2B (omitted $^{13}$C dimension). The diagonal shows the *ortho*-CH peaks, and contacts between *ortho*-CH sites and amide sites are visible as off-diagonal peaks. (c) Three-dimensional $^{15}$N-edited $^{1}$H-$^{1}$H RFDR experiment showing $^{1}$H-$^{1}$H spatial proximities from amide protons to amide and *ortho*-CH protons. The pulse sequence used was the same as in Figure S2B but with $^{13}$C and $^{15}$N channels inverted. (d) shows the respective diagonal peaks from panel (c) in a 2H $^{1}$H-$^{15}$N correlation spectrum. The latter was collected with a CP-based sequence, akin to the one shown in Figure S2A but with $^{13}$C and $^{15}$N channels inverted.

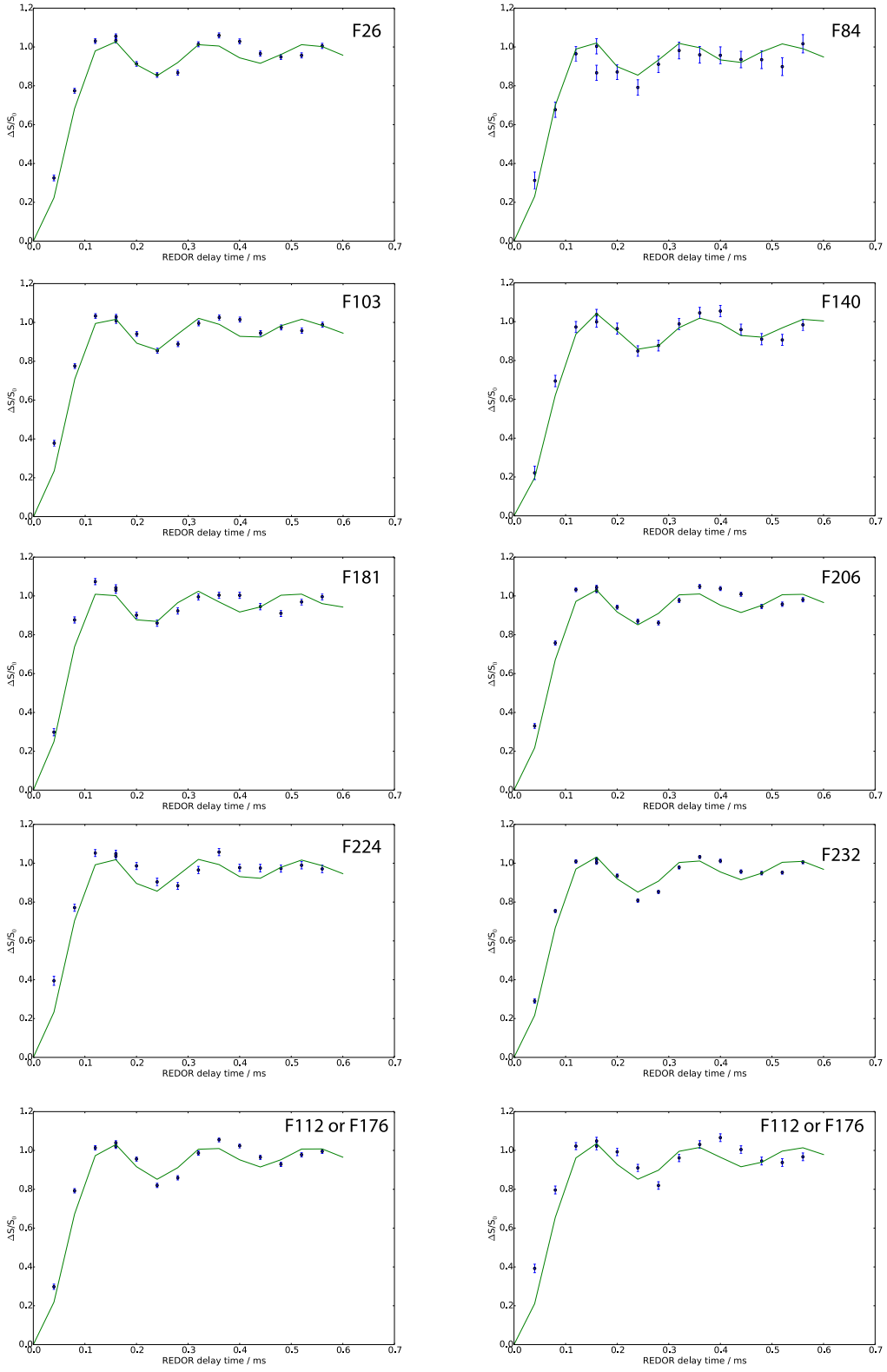


Figure S5. REDOR recoupling curves probing fast motion of *para*-CH sites in TET2. We note that in some cases the oscillation frequency observed experimentally and in simulations does not quite match. We do not have a definite explanation for this finding; possibly, more than one moiety may contribute to the experimental data, with overlapping resonance frequencies but distinct dipolar-coupling behavior. The uncertainty about the origin of this discrepancy does not alter the conclusion that these sites are rigid (fast dipolar oscillation) with high order parameters.

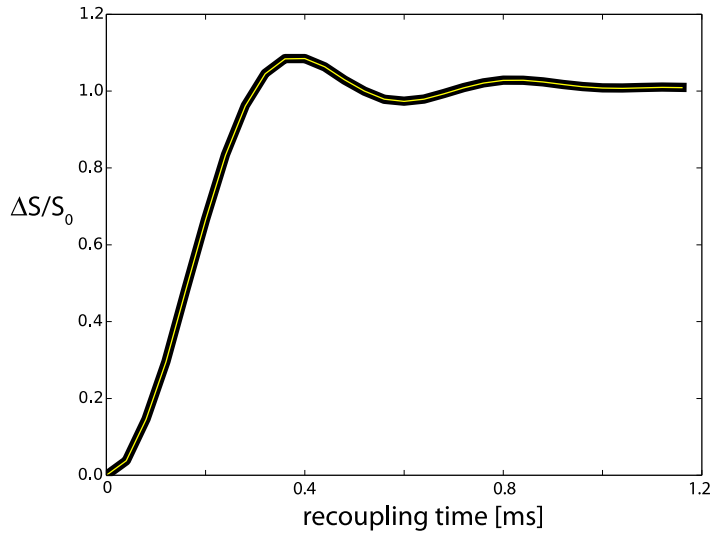


Figure S6. Effect of two-site jump motion on REDOR curves, investigated by numerical simulations of the REDOR recoupling using the GAMMA simulation library (*5*). The curve in black assumed a two-site exchange model in which a $^{1}$H-$^{13}$C site (dipolar tensor anisotropy 28.08 kHz, $^{13}$C CSA of $\Delta\sigma$=135 ppm (*6*) (20.25 kHz, collinear with the dipolar tensor) undergoes jumps between two sites. The simulation strategy was identical to the one previously used for methyl sites (*4*). The curve in yellow simulates the evolution under a dipolar coupling tensor and CSA tensor that are reduced by a factor of 0.625 (i.e., dipolar tensor anisotropy of 17.5 kHz) and the tensor asymmetry was set to 0.6. The match between these two curves shows that the two treatments, (i) explicit jump between two sites, or (ii) asymmetric dipolar tensor, are equivalent descriptions, as long as the two-site jump is the only motion present.

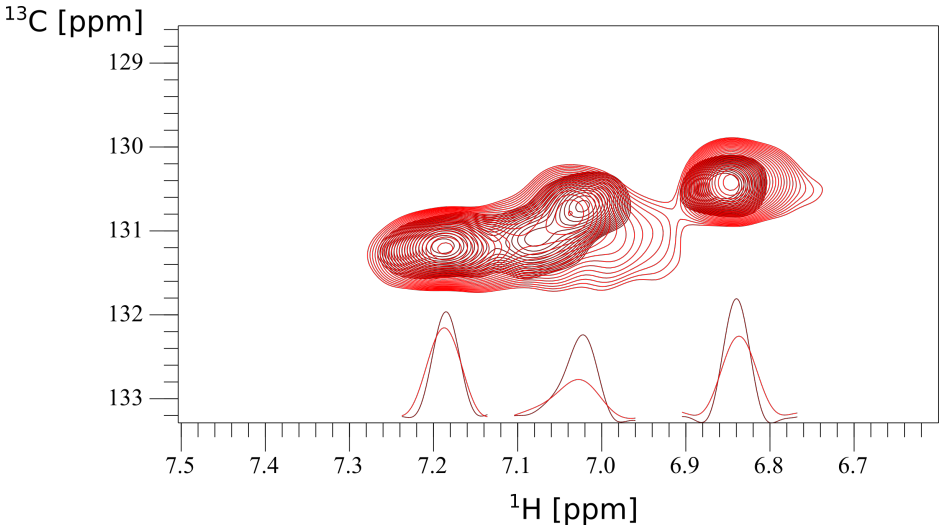


Figure S7. The temperature-dependence of the *ortho*-CH spectra at high temperature supports the notion that the four visible *ortho*-CH sites undergo changes on the "fast branch" (ns) of the $R_{1\rho}$ (or $R_2$) curve. Shown are $^{1}H$-$^{13}C$ spectra (CP-based) of *ortho*-CH labelled TET2 at temperatures of 25°C (red) and ca. 55 °C (brown). 1D traces at selected positions are indicated. The apparent sharpening of the lines at higher temperatures is explained by a shift from the tens-of-ns time scale to the low-ns time scale, where transverse relaxation is less efficient (cf. Figures 2H or S8).

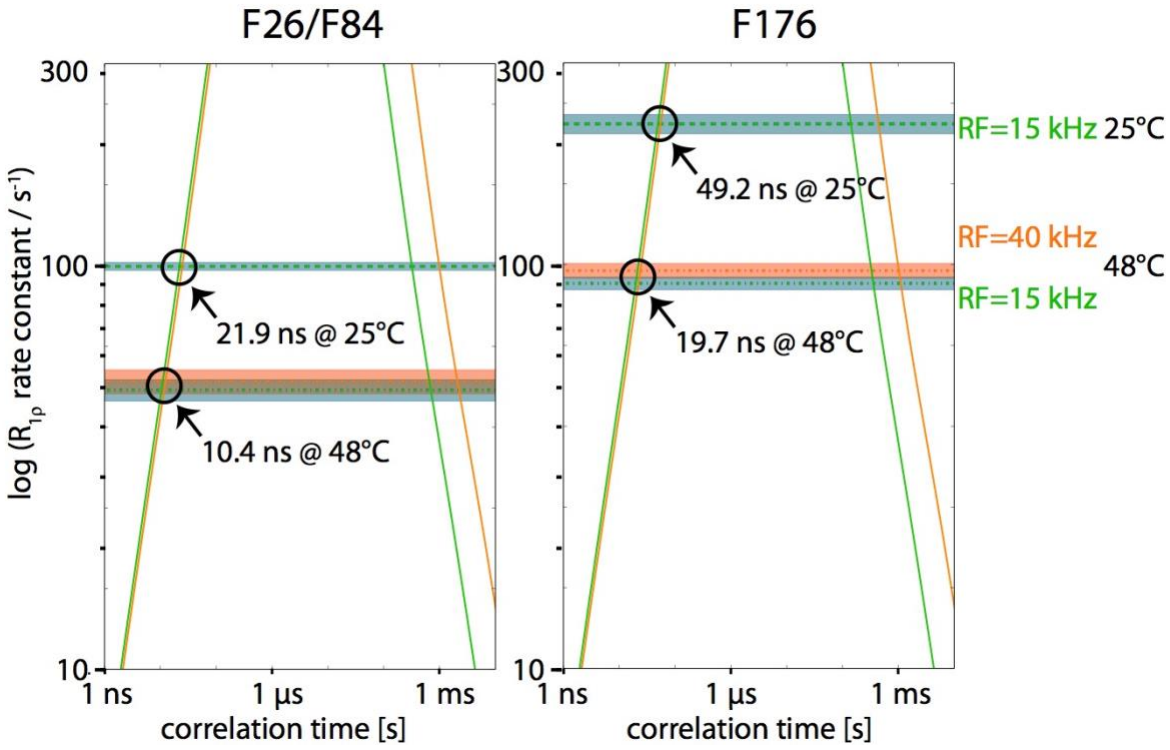


Figure S8. Estimation of the motional time scale of ring flips from ortho-CH sites. See caption of Figure 2H for details.

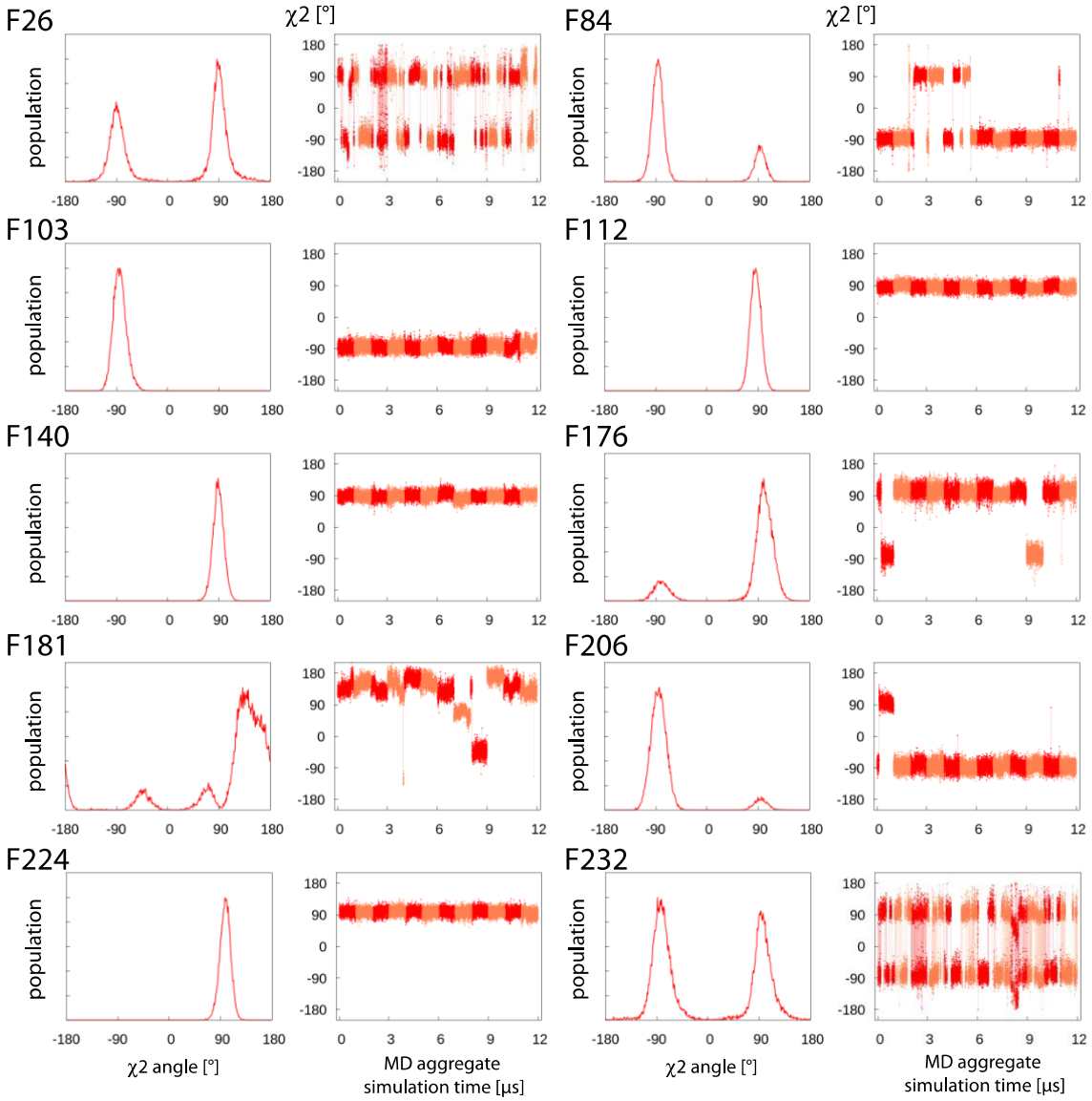


Figure S9. Ring flip motions of Phe residues in TET2 from a 1 µs-long molecular dynamics simulation of the dodecameric TET2 particle. Plotted are the time traces of the $\chi 2$ angle and the accumulated occupancy of the $\chi 2$ angles along the trajectory for the twelve subunits of the TET2 dodecamer. To better visualize data from different subunits, two different colors have been used in the time traces. Note that for the case of $\chi 2$, the population histograms on the left basically show the extent of convergence in the simulation, and ultimately the two populations are expected to be 1:1, as the two states are indistinguishable.

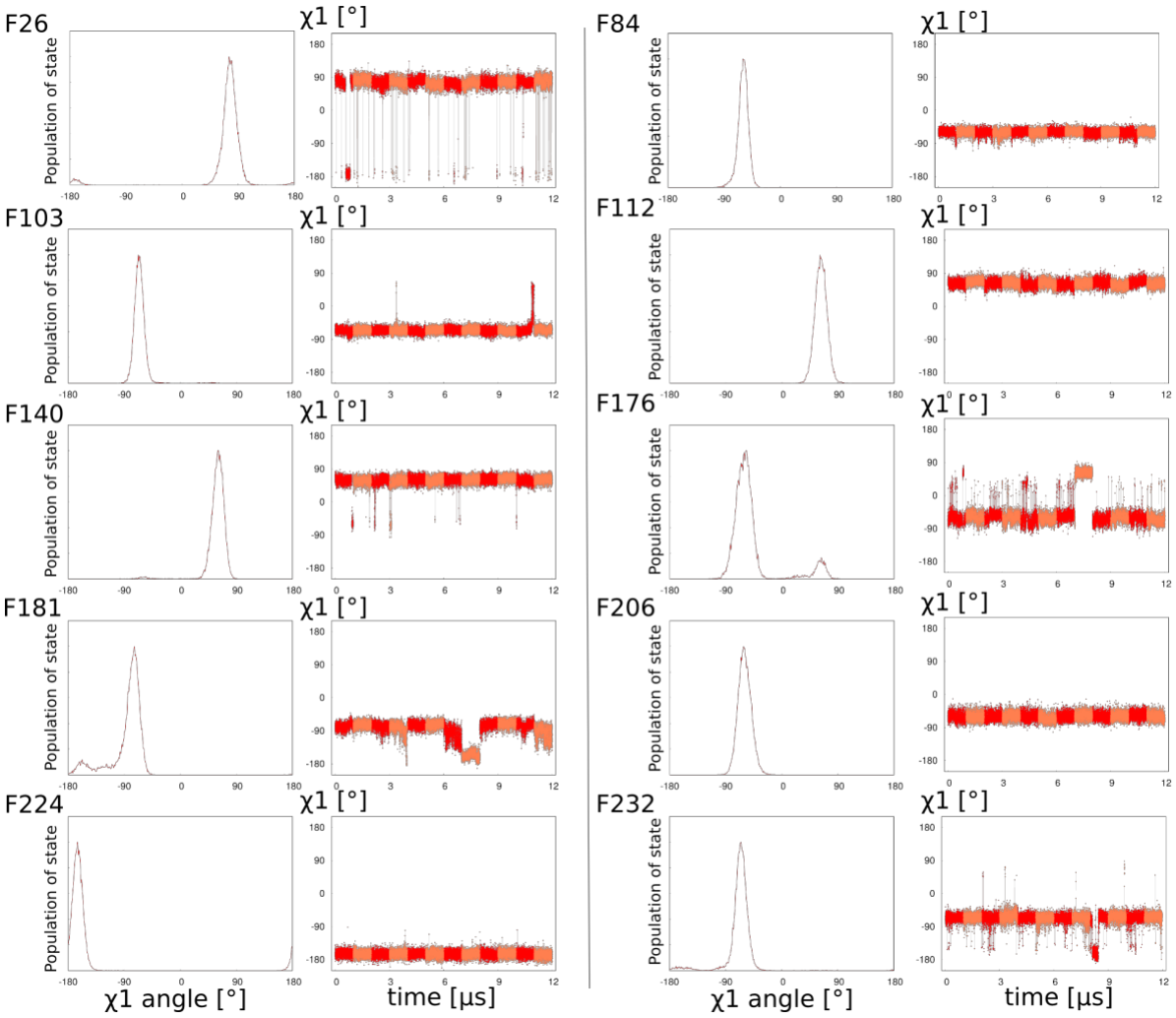


Figure S10. Ring axis motions (χ1 angle) of the Phe residues in TET2 revealed by MD simulations, plotted akin to the data in Figure S9.

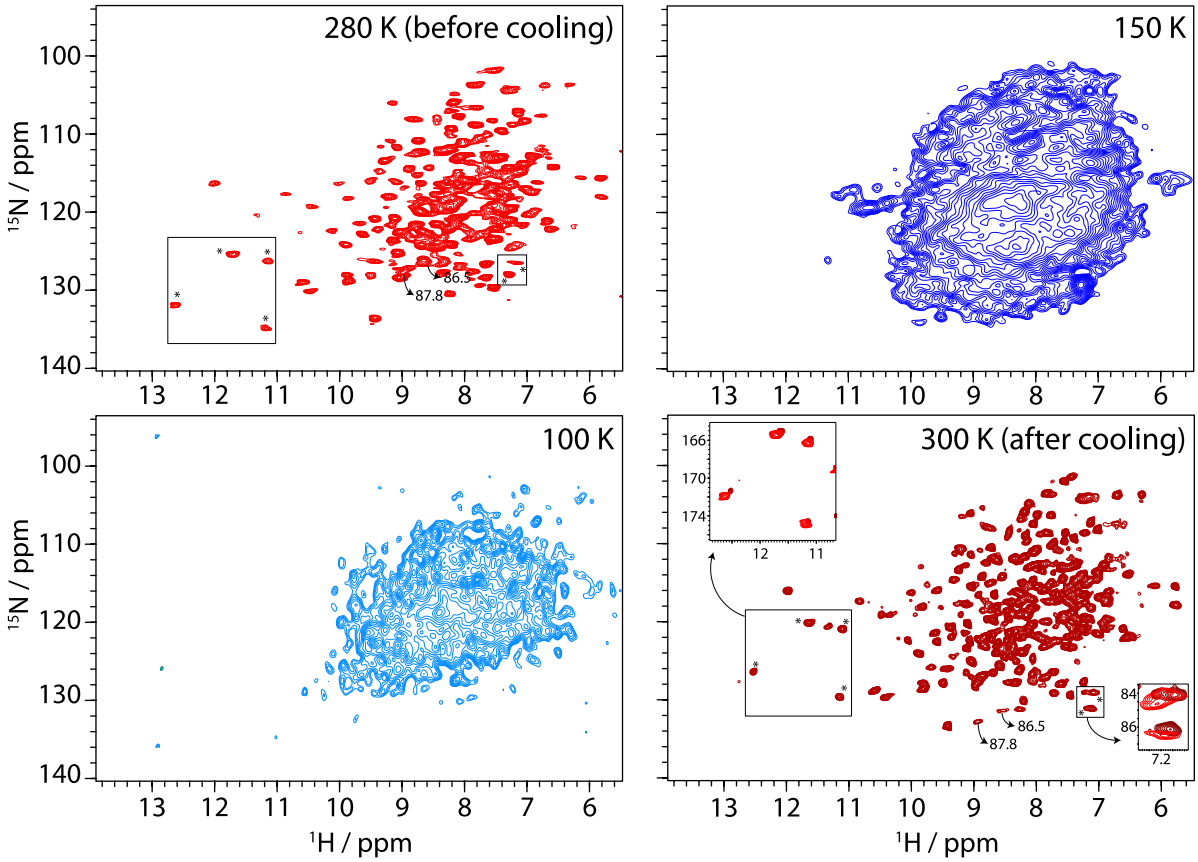


Figure S11. Proton-detected CP-based HN spectra of TET2 at different temperatures. The spectra at 280, 150 and 100 K were obtained at 800 MHz $^{1}$H Larmor frequency and a MAS frequency of 40 kHz, while the spectrum after the 100 K measurements was recorded on a 600 MHz machine at 50 kHz MAS and 300 K (lower right). Note that the peak positions before and after the 100 K measurements are very similar, showing that the temperature cycle does not considerably impact the sample. We ascribe the subtle changes to different $B_0$ field strength, temperature and MAS frequency. Several peaks are aliased spectrally, as they resonate outside the chosen $^{15}$N spectral range; they are folded differently in the two different high-temperature spectra due to different carrier/spectral width settings and thus appear at different positions. They are indicated in the lower right spectrum, along with two boxes showing their true resonance frequencies.

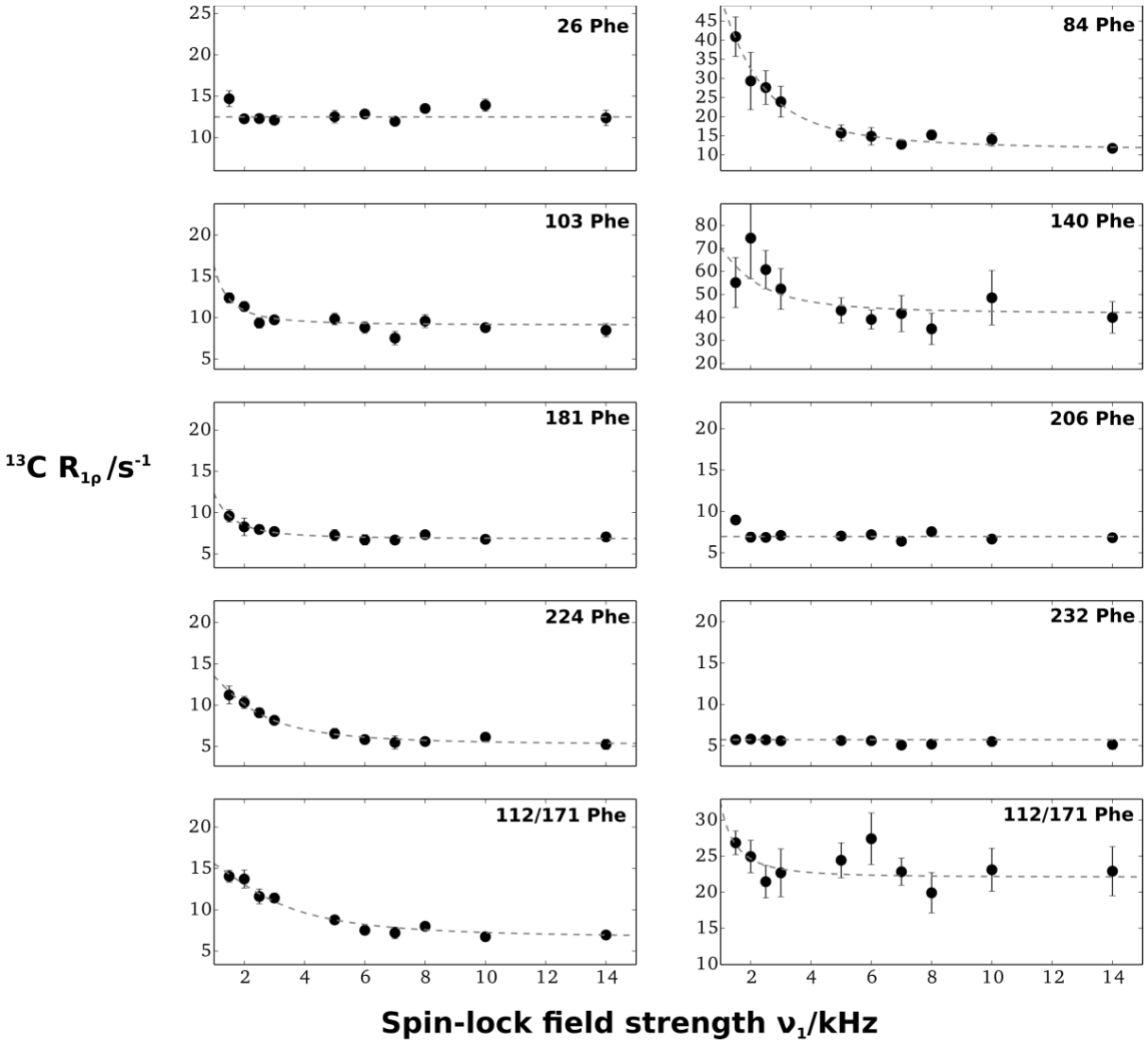


Figure S12. $^{13}C$ $R_{1\rho}$ relaxation dispersion profiles of *para*-CH sites in TET2.

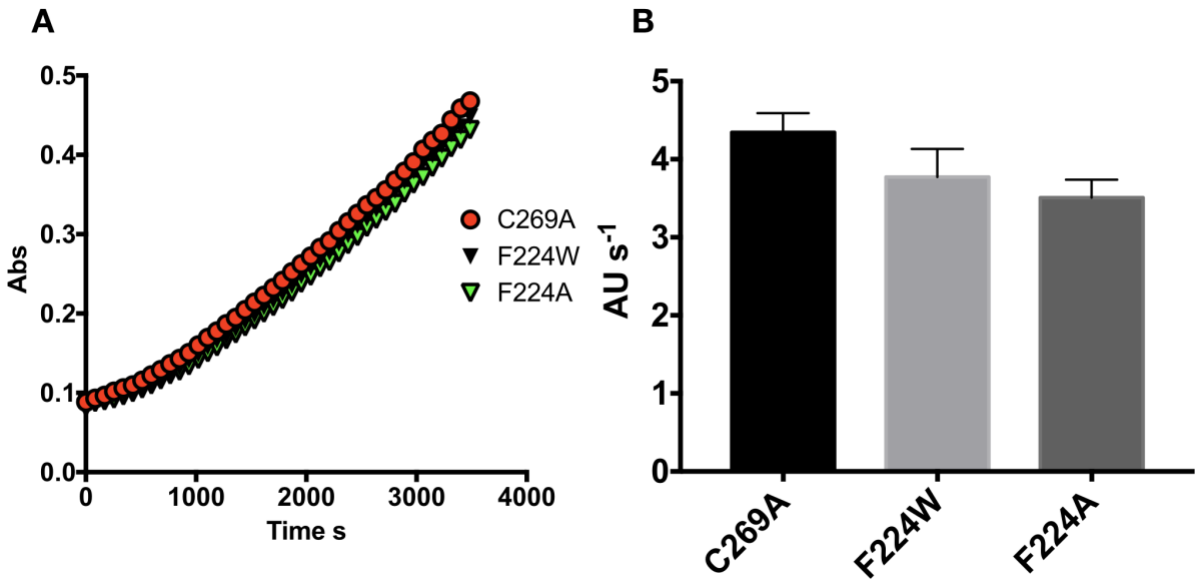


Figure S13. Peptidase activity of the TET2 mutants was measured using leucine-p-nitroanilide as a substrate. A) Representative curves showing the hydrolysis of the substrate and the resulting increase in absorbance at 410 nm wave length as a function of time. B) Initial rates averaged from 3 independent assays are compared. No significant difference is observed between a protein containing the native F224 and the two mutants, even though the differences between Trp and Ala in terms of occupied volume are substantial. (In the protein containing the native F224, a mutation of the Cys 269, over 20 Å from F224, was introduced in the context of of an unrelated study.) These data show that the volume occluded by F224, or its mobility, are not relevant for the activity of TET2.

References


1. R. Linser, B. Bardiaux, V. Higman, U. Fink, B. Reif, Structure calculation from unambiguous long-range amide and methyl 1H-1H distance restraints for a microcrystalline protein with MAS solid-state NMR spectroscopy. *J. Am. Chem. Soc.* **133**, 5905–5912 (2011).
2. M. J. Knight *et al.*, Fast resonance assignment and fold determination of human superoxide dismutase by high-resolution proton-detected solid-state MAS NMR spectroscopy. *Angew Chem Int. Ed. Engl.* **50**, 11697–11701 (2011).
3. J. D. Haller, P. Schanda, Amplitudes and time scales of picosecond-to-microsecond motion in proteins studied by solid-state NMR: a critical evaluation of experimental approaches and application to crystalline ubiquitin. *J. Biomol. NMR*. **57**, 263–280 (2013).
4. P. Schanda, M. Huber, J. Boisbouvier, B. H. Meier, M. Ernst, Solid-State NMR Measurements of Asymmetric Dipolar Couplings Provide Insight into Protein Side-Chain Motion. *Angew. Chem. Int. Ed.* **50**, 11005–11009 (2011).
5. S. Smith, T. Levante, B. Meier, R. Ernst, Computer simulations in magnetic resonance. An object-oriented programming approach. *J. Magn. Reson.* **106**, 75–105 (1994).
6. C. Ye, R. Fu, J. Hu, L. Hou, S. Ding, Carbon-13 chemical shift anisotropies of solid amino acids. *Magn. Reson. Chem.* **31**, 699–704 (1993).